Scale-free, programmable design of morphable chain loops of kilobots and colloidal motors

Mayank Agrawal[a] and Sharon C. Glotzer[a,b,c,1]

[a]Department of Chemical Engineering, University of Michigan, Ann Arbor, MI 48109-2136; [b]Department of Materials Science and Engineering, University of Michigan, Ann Arbor, MI 48109-2136; and [c]Biointerfaces Institute, University of Michigan, Ann Arbor, MI 48109-2136

Contributed by Sharon C. Glotzer, March 3, 2020 (sent for review December 24, 2019; reviewed by Aparna Baskaran and Michael A. Bevan)

Micron-scale robots require systems that can morph into arbitrary target configurations controlled by external agents such as heat, light, electricity, and chemical environment. Achieving this behavior using conventional approaches is challenging because the available materials at these scales are not programmable like their macroscopic counterparts. To overcome this challenge, we propose a design strategy to make a robotic machine that is both programmable and compatible with colloidal-scale physics. Our strategy uses motors in the form of active colloidal particles that constantly propel forward. We sequence these motors end-to-end in a closed chain forming a two-dimensional loop that folds under its mechanical constraints. We encode the target loop shape and its motion by regulating six design parameters, each scale-invariant and achievable at the colloidal scale. We demonstrate the plausibility of our design strategy using centimeter-scale robots called *kilobots*. We use Brownian dynamics simulation to explore the large design space beyond that possible with kilobots, and present an analytical theory to aid the design process. Multiple loops can also be fused together to achieve several complex shapes and robotic behaviors, demonstrated by folding a letter shape "M," a dynamic *gripper*, and a dynamic *pacman*. The material-agnostic, scale-free, and programmable nature of our design enables building a variety of reconfigurable and autonomous robots at both colloidal scales and macroscales.

active particles | colloidal robotics | design | kilobots | morphological control

Applications for autonomous robotic machines operating on submicron scales are foreseen in healthcare (1), defense (2), manufacturing (3), and programmable matter (4). A key feature of such machines is their ability to morph into preprogrammed configurations in response to a stimulus. Two major attributes of robotics on any length scale are actuation and control. Conventional robotics uses electromechanical actuation components; this is challenging at small scales, due to fabrication limitations, presence of stochastic forces, material constraints, or the need for biocompatibility (3, 5, 6). One approach to achieving actuation on microscopic scales is to exploit physicochemical principles of colloidal science. In this approach, colloidal motors on the order of hundreds of nanometers to several microns—also known as active particles—convert energy in their environment, such as light, chemical fuel, heat, sound, and electric and magnetic fields (7–12), into a propulsion force (5, 7–9). Active particles can be made from a variety of materials, including metals, polystyrene, silica, polymethyl methacrylate (PMMA), polydimethylsiloxane (PDMS), and hydrogels (5, 7–9), and in many different shapes, such as spheres (13), rods (8, 9), and gears (10). Examples of active particles include molecular motors (14, 15), microorganisms (8), self-propelling (13) and self-rotating colloids (10), and particles propelled via symmetry breaking (16, 17). Propulsion speeds ranging from microns to tens of millimeters per second have been demonstrated (8). Such diversity in material, shape, motion, and method of actuation, combined with the ability of colloidal particles to self-assemble, renders active particles ideal motors for submicron applications.

Colloidal robotic machines aim to achieve some of the same behaviors as conventional swarm robotics, but in a very different way. In swarm robotics, the distributed control logic of robots (individual motors) is programmed via local interactions between the motors. An excellent example is provided by *kilobots*, fist-sized motors with their own control logic and memory on board. Rubenstein et al. (18) proposed an algorithm that runs on every kilobot, enabling them to self-organize as a swarm into prescribed shapes. A critical feature of that approach is that each kilobot knows the target shape and, through communication with other kilobots, its location in the shape. Such knowledge would be challenging to imprint on a colloidal particle, and, therefore, active colloidal systems typically form emergent patterns rather than finite shapes (9, 13, 19). Hence, we seek an approach to make finite colloidal machines but with nonintelligent particles that lack individual identity.

One such approach is morphological control, where the physical relation between different elements of a system control its behavior. Hence, the information of the function is stored in the design of the system's structure. This presence of structure is absent in the swarm systems, which allows morphological systems to encode relatively more information. For instance, proteins, the workhorses of living organisms, are chains of amino acids, which have 20 different varieties. Different amino acids in a protein interact among themselves in a unique fashion due to their particular sequence, thereby storing information about their function in their sequence. Four-dimensional (4D) printing is another rising field in this context, where structures are

Significance

Researchers have synthesized many different types of colloidal particles that can convert an external stimulus into propulsion capable of propelling the particles, thereby making them "active." The availability of active particles motivates building colloidal machines with controllable behavior. In biology, proteins are colloidal-scale machines that possess controlled morphing behavior as encoded in the sequence of their amino acids; this is an example of morphological control. Inspired by this idea, we show how to build finite colloidal machines that can morph and reconfigure their structure using active particles. The information that dictates the morphing behavior is encoded in the system by chaining sequences of active particles into loops, creating a type of colloidal robot.

Author contributions: M.A. and S.C.G. designed research; M.A. performed research; M.A. analyzed data; and M.A. and S.C.G. wrote the paper.

Reviewers: A.B., Brandeis University; and M.A.B., Johns Hopkins University.

The authors declare no competing interest.

Data deposition: All data as well as simulation, analysis, and visualization scripts are publicly available at https://doi.org/10.7302/czgw-2x26. The software used to perform the simulations is publicly available at https://github.com/glotzerlab/hoomd-blue.

[1]To whom correspondence may be addressed. Email: sglotzer@umich.edu.

This article contains supporting information online at https://www.pnas.org/lookup/suppl/doi:10.1073/pnas.1922635117/-/DCSupplemental.

First published April 7, 2020.

printed with different inks, each with a different response to, for instance, temperature. The pattern of different inks decides the system's morphological response to the stimuli temperature (20). Li et al. (21) developed a system using macroscale robots that actuate by swelling and contracting, which pushes and pulls neighboring robots. The robots are programmed to actuate out of phase with each other; this phase offset programs the dynamical behavior of the system. These particle robots also require basic computation and clock synchronization. While colloidal particles can be made to swell or contract with an environmental change, such as a change in temperature or solvent pH, achieving programmable actuation with a prescribed phase for each individual, essentially identical, particle is still not feasible. Instead, colloidal robotics must rely upon identical interparticle interactions. This was demonstrated recently by Slavkov et al. (22), who programmed interactions between their robots via chemical signaling to achieve simple shapes with appendages. Their system is robust, but the target shapes lack the variety and precision we seek for submicron-scale robotic applications. Another system of identical particles is bristle bots (23). Bristle bots can move and spin and interact through mechanical collisions to form dynamic phases. The translation to spin ratio is varied to tune the dynamic behavior. The natural limitation of using independent identical robots without the onboard ability to carry and process information is that they can only achieve a small number of static and dynamic behaviors.

In the growing number of studies of macroscale or colloidal-scale robots, the robots are free to move relative to one another, other than a confining boundary so they do not fall off the table or leave the simulation box. However, it is now possible to link together colloidal particles with, for example, polymers (24) or DNA oligonucleotides (25–27) of nearly arbitrary length and stiffness. Motivated by these developments and the possibility of particle chaining, here we present a design approach (Fig. 1*A*), implementing morphological control, to program a system of nonintelligent motors (i.e., lacking onboard logic) into precise, preprogrammed behavior. We use motors that mimic active particles through constant forward propulsion. The novelty of our design is to connect the motors end-to-end in a loop such that each robot's propulsion force direction is always tangential to the loop. Each connection between neighboring motors is a hinge that allows relative rotation only in the plane of the loop, constraining the possible behaviors to two dimensions as in the examples above. The only intermotor interaction beyond steric interactions is this mechanical constraint, and thus programmability of the steady-state loop shape (and subsequent behavior) is dictated by motor self-propulsion subject to these constraints, and the sequencing of motors along the loop. These motors do not employ any other form of communication and computation of the kind used in systems of Rubenstein et al. (18), Li et al. (21), and Slavkov et al. (22). Connecting colloids into chains has been investigated before with a focus on the filament dynamics, mechanical coupling, and relation to polymer scaling theory (28–30). However, these are nonloop chains with all particles similarly oriented along the chain, which is why the information encoding is limited. Through our system, we extend the focus of active colloidal chains toward robotics by introducing a programmable architecture. An approach toward programming chains is demonstrated by Spellings et al. (31), where they link gear-shaped particles with rotational motion in a loop. The loop also encapsulates passive particles. The alternating sequence of clockwise and anticlockwise spinning particles interacts with the passive interior to symmetrically buckle the boundary. Our system uses particles with translational motion to extend and develop the notion of programmability for active loops. We perform experiments with several designs using kilobots to establish proof of concept, and use Brownian dynamics simulations to explore the rich design space and demonstrate the scale invariance of our approach. We discuss the morphing mechanism as a consequence of three driving forces, which, in turn, are derived from the force interactions in the loop, and we provide a design procedure to reverse-engineer the loop design for a given target shape. Beyond simpler behaviors, we demonstrate complex behavior using examples like *pacman* (dynamic behavior) and the letter "M" (static behavior) by decomposing the designed loop into simpler components and then combining them. To quantify the mechanical stability of the loop configuration, we present an analytical solution of the loop dynamics (see *Theory*), which also allows for quick estimation of forces and velocities on different loop configurations.

Six design parameters govern the force interactions (illustrated in Fig. 1*B*) and allow programmability. These are 1) motor orientations with respect to the loop, 2) relative strengths of each motor's propulsion force, 3) relative motor sizes, 4) the strength of stochastic forces on the motors, 5) loop size, and 6) internal pressure within the loop. The length and force quantities in the design parameters are nondimensionalized using the motor length and the bond strength of the hinge, respectively, which are both constant along the loop (see details in *Simulations*). The system's design can be scaled by defining the scale of these parameters. This implies that, while scaling, the number of motors in the loop, that is, the loop size and their sequence

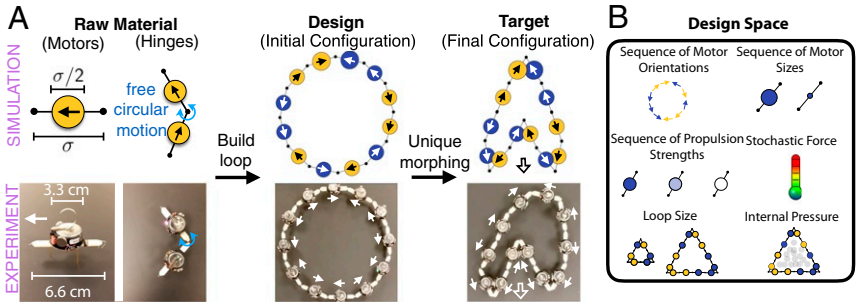

Fig. 1. System overview. (*A*) Constantly propelled motors are sequenced end-to-end in a loop using our design strategy to fold an arrowhead shape (Movie S1). Each motor can be arranged to point its propulsion in one of the two directions with respect to the loop (shown using arrows and yellow/blue colors for the simulation, and white arrows for the experiment). Design parameters for the shown loop are as follows: motor orientations as colored; propulsion strength is identical on all motors; for simulation, motor widths are $\sigma/2$ except for the two larger motors with width 0.6 σ (analogous steric effect is obtained between the corresponding kilobots by shaping popsicle stick ends [*SI Appendix*, Fig. S1], described in *Materials and Methods*); stochastic force is low ($\bar{T} = 0$ for simulation); loop size is 12 motors; and internal pressure is zero. (*B*) Design parameters of the loops. These determine the steady-state behavior of the loop.

of orientations, remains fixed. When it was not possible to use the same number of motors, the same shape as in the simulation was achieved in the experiments by reproducing a coarse-grained version of the sequence with fewer motors. The exact force scaling is difficult with kilobots because their propulsion calibration is imprecise and limited. Hence, we implement the simplest form of force distribution for the kilobot loops that correspond to their colloidal counterparts (described in *Kilobot Experiments*). Our scheme can achieve the complex emergent behavior schematically drawn in Fig. 1*B*. The external stimuli controlling these design parameters can be used as both the power source and the communication agent for controlling the loops. In this way, multiple responses can be programmed using a single set of design parameters to achieve either autonomous (environment response) or user-operated (external field response) smart behavior.

Kilobot Experiments

We describe the basic design strategy by sequencing kilobots to form the *gripper* robotic machine shown in Fig. 2. Each kilobot is programmed to constantly propel forward to mimic a colloidal motor. All kilobots possess similar propulsion strengths. A small amount of stochastic force is introduced in the propulsion program (see *Materials and Methods*). This stochasticity is very low, and, hence, the kilobot loops fold as if in a nonthermal regime. Loops are created by chaining kilobots together with popsicle sticks. At the simplest level of design, there is one stick between every two kilobots. Additionally, we can replace a kilobot with a popsicle stick (see *Experiment*), so that each motor exists in a ternary state—two states for orientation and a passive state (when the kilobot is replaced by a stick)—and the combinatorial permutations of active and passive kilobots provides programmability. When two kilobots are linked facing in opposite directions with a passive bot between them, their propulsion stretches them into a straight chain (shown in Fig. 2*A*). This property is used to form straight segments of a shape. Fig. 2*B* shows a triangle folded using three such segments. Substituting a kilobot in one of the segments (Fig. 2*C*) with a passive stick introduces a net force on that segment to form a curved triangle with net rotation. To build a gripper, two such triangle sequences are fused at a vertex as shown in Fig. 2*D*. Gripping behavior can be achieved by switching between passive and active states of the two corresponding motors. In Fig. 2*E*, we illustrate a noninvasive surgery cartoon as a robotic application where the closed and open gripper states are controlled by two different light sources. We demonstrate operations like gripping and incising (Fig. 2*E*) using kilobots and foam blocks (Movie S2).

In Fig. 3 (Movie S3), we show several folded shapes achieved by using up to 12 kilobots. The arrowhead shape shown in Fig. 1*B* (Movie S1) and Fig. 3*C* features a notch. Achieving this notch under low stochasticity requires an additional design parameter, local angle constraints. One way to achieve this is by replacing some kilobots with larger motors, as shown in simulation snapshots (Figs. 1*B* and 3*C*), which increases the minimum angle possible between neighboring bots without steric hindrance (the role of this steric hindrance is discussed in *Folding Mechanism*). Because all kilobots are the same size, we tune the minimum angle between kilobots by shaping the ends of the popsicle sticks connected to them (see *Experiment* and *SI Appendix*, Fig. S1). The distorted folding of the arrowhead compared to its simulated counterpart is due to the imprecise nature of the kilobots. These demonstrations using kilobots—a relatively primitive "active particle"—demonstrate the plausibility of our design approach.

Active Particle Simulations

Extending the design space to all six parameters using simulations achieves a wider variety of shapes and motions (Fig. 3 and Movie S4). To demonstrate this, we use Brownian dynamics simulations, a standard technique for studying active colloids that mimics their stochastic Brownian motion in solvent (see *Simulation*). The key morphological and dynamic features of the loop shapes designed and demonstrated in simulation are 1) straight and curved segments of variable length, 2) zigzag pattern, and 3) net translation or rotation. All of the shapes in Fig. 3 are stable under thermal (Brownian) forces. The target space of loop morphologies and behaviors extends to more complex robotic

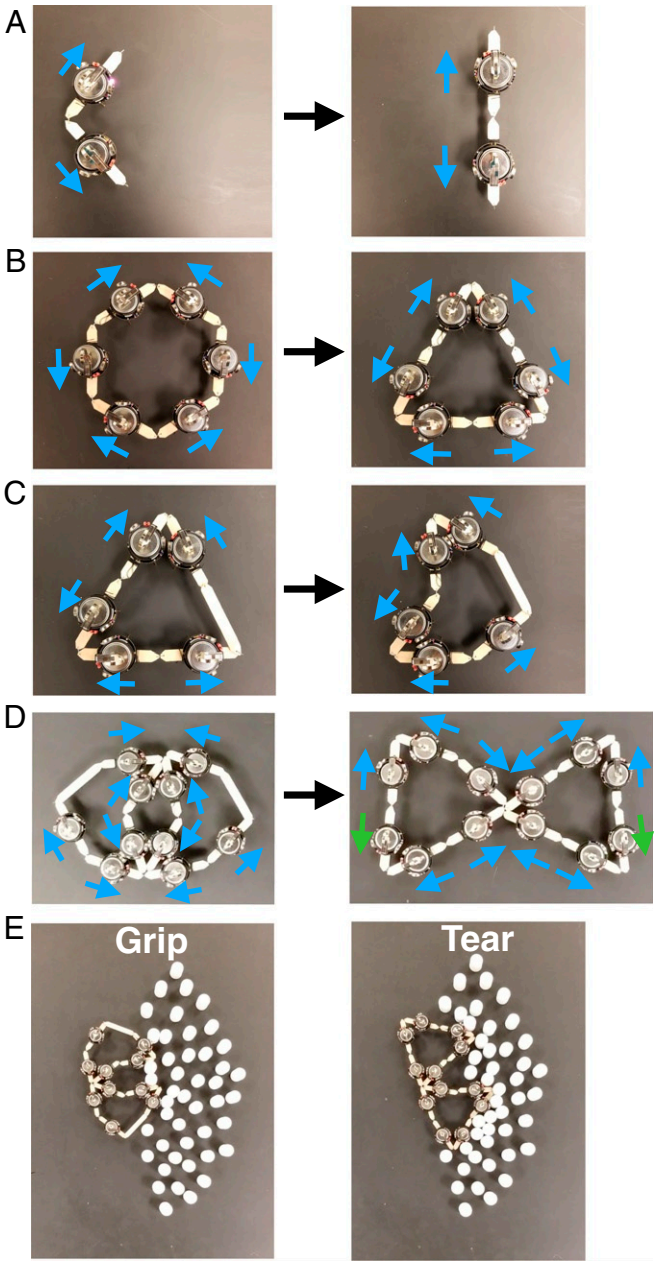

Fig. 2. Sequencing of kilobots. (*A*) Two kilobots with diverging propulsion at their joint straighten. (*B*) Loop composed of three segments each with the sequence shown in *A* folds into a triangle. (*C*) Replacing a kilobot of the triangle in *B* with a stick (passive state) generates net force driving the curving and rotation of the triangle. In *A–C*, *Left* and *Right* are the initial and final configurations, respectively. (*D*) The gripper composite is formed by connecting two of the loops in *B* and *C*. Switching between the active and passive state of the two motors (green arrow) achieves the closed (*Left*) and open (*Right*) states of the gripper. The arrows in *A–D* indicate the corresponding kilobot's direction. (*E*) Experimental demonstration showing the gripping and tearing operations on foam blocks (Movie S2).

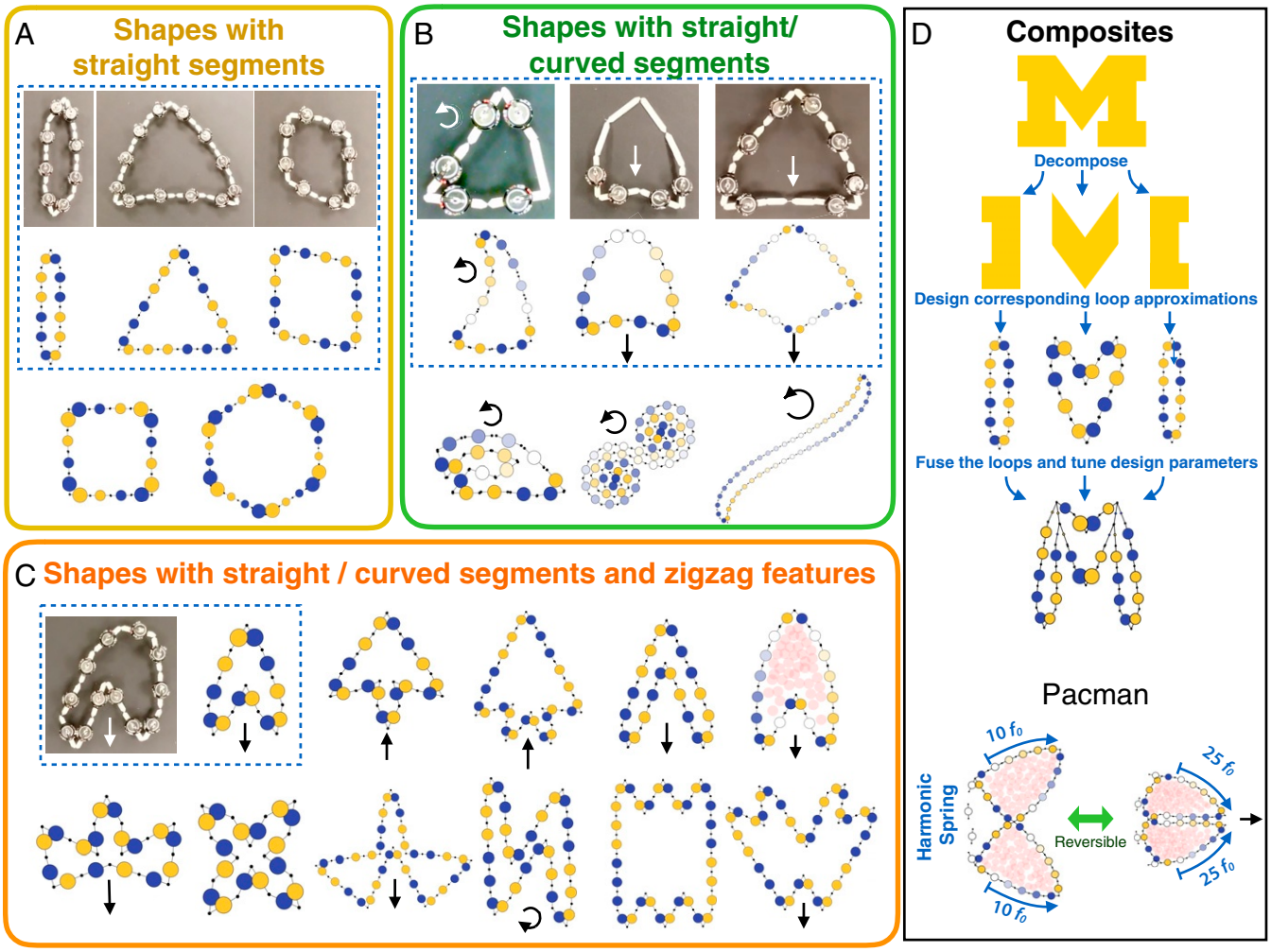

Fig. 3. Example range of targets. Our design scheme achieves shapes that can be constructed as straight or moderately curved lines (segments) connected at corners. (*A*–*C*) Simulation snapshots of example shapes in increasing complexity. The key morphological features of these shapes are straight segments, curved segments, zigzag geometry, and net motion. The straight or curved arrows indicate the shape's net translation or rotation if present. Dashed blue line encloses simulation and experiment version of shapes. All shapes are stable at ($\overline{T} = 0.1$), although shapes in *A* and those corresponding to experiments do not require stochasticity to fold. The graded color opacity along some subsegments—sets of similarly colored consecutive motors—indicates linearly increasing propulsion magnitude. (*D*) Composites are multiple loops fused together and can achieve more complex behavior such as the letter "M" (design procedure is shown, simulation snapshot is shown at the bottom), and pacman. Simulation snapshots of the two states of pacman are achieved reversibly by tuning the net propulsion strength of the two subsegments as shown. Harmonic spring is a chain of passive (white) motors bonded with harmonic coefficient 0.002 k_0. Reversible switching between the two states resembles the Pac-Man behavior. See *SI Appendix*, Figs. S2 and S3 for the complete design parameters, and see Movies S3 and S4 for the movies.

behavior by fusing multiple loops together into composites. In addition to the gripper example discussed above, Fig. 3 shows two more examples. The first example is the morphing of the loop into the letter "M" (Movie S5). The second example is a pacman shape (Movie S6), which uses two loops similar to the gripper but is more sophisticated. The closed state produces the net forward motion of the loop. Switching repeatedly between small and large propulsion strengths drives the system to reconfigure repeatedly between open and closed states while also propelling the robot forward in a way that resembles the arcade game character Pac-Man.

Design Procedure

The design procedure we employed to achieve the above results comprises four distinct steps (illustrated in Fig. 4), which can be used to generate any 2D shape.

In step 1, the target shape is simplified to a set of straight or curved line segments connected end-to-end at corners. Each line segment corresponds to a loop segment. The number of loop segments is determined by the desired resolution of the morphological features. We start from the minimum possible number of motors to minimize the loop's complexity. As a heuristic, the shortest segment is set to contain two motors, and then the sizes of other segments are relatively chosen to correspond to the target shape. If required, the motors can be added segment-wise as described in *Varying Loop Size*. While adding more motors, the loop's symmetry features are maintained. In Fig. 4*A*, we consider two examples: an arrowhead, with all straight segments, and a curved triangle, with two bends and one straight segment.

In step 2, the orientations and propulsion strengths are sequenced segment-wise. Straight segments are formed by placing two sets of motors, or subsegments, facing in opposite directions such that they pull away from each other as shown in Fig. 4. We use equal numbers of motors and equal propulsion forces in both subsegments. If the segment size has an odd number

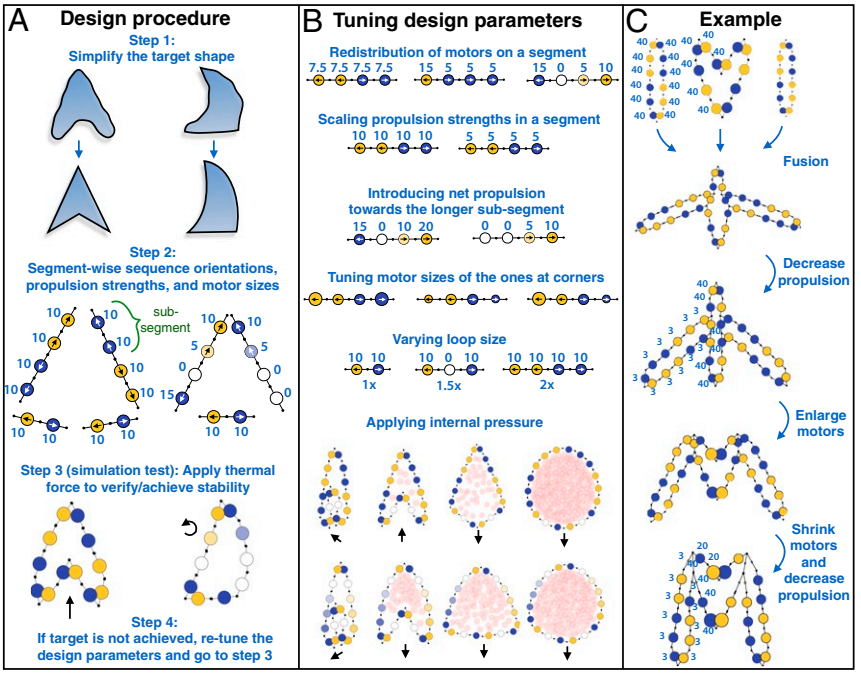

Fig. 4. Design procedure. (*A*) Shown is the general design procedure of identifying and tuning the design parameters given the target shape. *Right* and *Left* follow the design for the two target shapes. This strategy generates a segmentation of the loop for the given target shape. (*B*) Illustration of the heuristics for retuning of the parameters, which is performed segment-wise. Bottom two rows show simulation snapshots of two loops with different internal pressure (*SI Appendix*, Fig. S4). Internal pressure is induced by adding soft particles inside the loop (see *Materials and Methods* for details). The numbers and internal arrows, if shown for the motors, are their propulsion strengths (in units of f_0) and orientations, respectively. (*C*) Parameter tuning for the letter "M" (shown in Fig. 3).

of robots, we use a passive motor in the middle (see example in Fig. 4*B*).

To achieve curved segments, the two subsegments are placed facing in opposite directions. With one of the subsegments longer than the other, the segment can curve. Then, by linearly increasing the magnitude of the propulsion force along the subsegment, its optimal stability is achieved when curved (discussed in *Folding Mechanism*). By having a larger propulsion force on the longer subsegment as compared to the shorter one, the curved segment is propelled forward in the direction of the net force (Fig. 4*A*).

In step 3, we verified that the target shape folds into the desired shape and is mechanically stable under stochastic forces. For several shapes, thermal forces are apparently required for folding (shown in Fig. 3, discussed in *Folding Mechanism*). Fig. 4 shows the simulation results of two designed loops in step 3.

In step 4, in the event that the target shape does not form, or is unstable, retune the design parameters as described in the next section and return to Step 3.

Tuning Design Parameters

We found that the following heuristics help to navigate the enormous design space (illustrated in Fig. 4*B*). The first five heuristics operate segment-wise. These change the force interactions between the segments, which may vary the folding dynamics and hence the stable, steady-state configurations. When tuning these design parameters for a loop configuration, the analytical solution, developed using rigid body dynamics and given as $\dot{\boldsymbol{\theta}} = f(\boldsymbol{\theta})$, where vector $\boldsymbol{\theta}$ describes motor orientations, can be used to estimate the changes in the loop's folding pathway and to calculate the target shape's mechanical stability. Understanding of the loop folding mechanism provides further intuition for tuning design parameters. In *SI Appendix*, Fig. S5, we show variations of the arrowhead shape achieved along different dimensions of the design space.

Redistribution of Motors on a Segment. The relative number of motors in the subsegments can be varied while maintaining the net propulsion force of each subsegment. For a subsegment, all motors have identical propulsion directions and may have either identical or linearly increasing magnitude.

Scaling Propulsion Strengths in a Segment. The propulsion strength of each motor in a segment is scaled by a constant factor.

Introducing Net Propulsion toward the Longer Subsegment. Given that one subsegment is longer than the other one and possesses linearly increasing propulsion strength, it can possess propulsion larger than the other subsegment. This can be achieved by scaling up or down the propulsion forces on the longer or the shorter subsegment, respectively.

Tuning Motor Sizes at Corners. The widths of the motors determine the minimum fold angle. The steric interactions governing the folding dynamics arise from the motors at the shape's corner, that is, the motors at the ends of each segment. Therefore, the sizes of only these motors need to be tuned. In simulations, we vary the diameter of the central particle in a motor, and, in experiments, we shape the ends of the kilobot's stick (see *Materials and Methods* and *SI Appendix*, Fig. S1).

Varying Loop Size. While all previous heuristics can be applied independently to a segment, every segment is scaled alike to vary the loop size. Given the scale factor of the loop size, each segment is scaled by maintaining the relative ratio of the number of motors in the subsegments. If required, a passive motor between subsegments can be used to maintain this ratio. If that is not possible, the motors can be redistributed using the first heuristic.

Applying Internal Pressure. Encapsulating soft particles within the loop provides internal pressure, which additionally stabilizes

different morphological features in the same loop. Fig. 4*B* (rows 6 and 7) demonstrates this for two types of loop sequences. Without any internal pressure, the two loops fold into similar arrowhead shapes, although with different net motion. A slight increase in internal pressure leads to bulkier arrowheads, with a noticeable difference between the two. Further increases in pressure produce polygons, and, eventually, circles. At the colloidal scale, internal pressure can be created in multiple ways, such as stimuli-responsive particles within the interior of the loops that swell in response to external stimuli such as light, pH, or moisture (32); increasing electrostatic repulsion between the motors along the loop; or activating an equal propulsion force on each motor along the local normal direction. The last mechanism can also be implemented for the macroscale loops, although we did not perform such experiments with kilobots.

Stochastic Force. Stochastic forces drive the loops to explore more of configuration space than is possible with only deterministic forces. The propulsion forces maintaining the loop in its steady-state shape restrain this exploration. The higher the temperature relative to the propulsion strength, the larger the amount of configuration space explored, which can assist in folding the target shape, switching between different shapes, and destabilizing the shape (discussed in *Folding Mechanism*).

Composites. Complex shapes, such as the letter "M," demand many segments and more time to fold, and may possess multiple mechanically stable configurations resulting in a nonunique steady state. Some complex behaviors, such as the gripper and pacman examples, may not be feasible using a single loop. Also, complex single loops are generally less stable, as we will see in *Quantifying Stability of the Folded State*. Hence, issues of infeasibility, degeneracy, slow relaxation, and low stability can potentially be avoided by using composites, where multiple loops are fused together, each sharing some part of their loop with the other (Fig. 3). Compositing adds topological constraints that modularize parts of the loop, and hence, for shapes with many features, compositing may yield more reliable folding. The procedure to design composite loops is illustrated in Fig. 3 using the example of the letter "M." First, the "M" is decomposed into simpler shapes. The number of these shapes depends on the desired resolution of the target, which is three for this example. The loops for these shapes are identified using the design procedure. Here, we need two rod-like loop shapes and an arrowhead loop shape. Finally, the loops are fused, and the design parameters are retuned to achieve the target.

Fig. 4*C* shows the tuning of parameters for the letter "M." Starting from the composite of the sequences of two rod-shaped loops and an arrowhead loop, each motor was assigned a constant propulsion speed of $40\ f_0$. We observed that, with this value, the rod-shaped loops form fast but spread wide. We then decreased the propulsion strengths on the rods to $3\ f_0$. We also increased the size of certain specific motors (as shown), which helped form the arrowhead (V-shaped) loop in the center of the letter. Further fine-tuning of specific motor sizes and propulsion strengths achieved the target letter shape. For the pacman (Fig. 3*D*), the lobes were filled with passive bots to provide internal pressure, sustaining the rounded morphology and increasing stability in the closed state. Harmonic springs were used to produce the open state. See *SI Appendix*, Fig. S3 for the complete design parameters of the three composites, and see Movies S5 and S6 for the movies.

Loop Motion. The motion of the folded shapes results from the loop sequence of the motors and thus the net propulsion force on the loop, which can be calculated a posteriori in simulations or a priori using the analytical solution. Naturally, any net motion will be along the asymmetric axis (Fig. 3). There are (at least) three ways in which a loop can be moved (shown in Fig. 5). The first way is by tuning the design parameters. For instance, enlarging motors of the arrowhead loop in Fig. 3*A* reverses the motion (Fig. 5, *Left*). The second way is by assigning to each motor an additional propulsion force biased in the desired direction (Fig. 5, *Center*). A third way is to attach an external navigator to the loop, such as a magnetic navigator controlled via an external magnetic field (Fig. 5, *Right*).

Reconfiguring between Different Folded States

Reconfiguration between folded shapes proceeds by switching between the respective design parameters of each shape. In some cases, switching the parameters of one folded shape can directly reconfigure it into the second folded shape. We refer to these as direct reconfigurations (*SI Appendix*, Fig. S6). In general, however, loop folding depends on the starting configuration, and thus direct reconfiguring from one arbitrary configuration to another may not be possible or may lead to a mechanically trapped state.

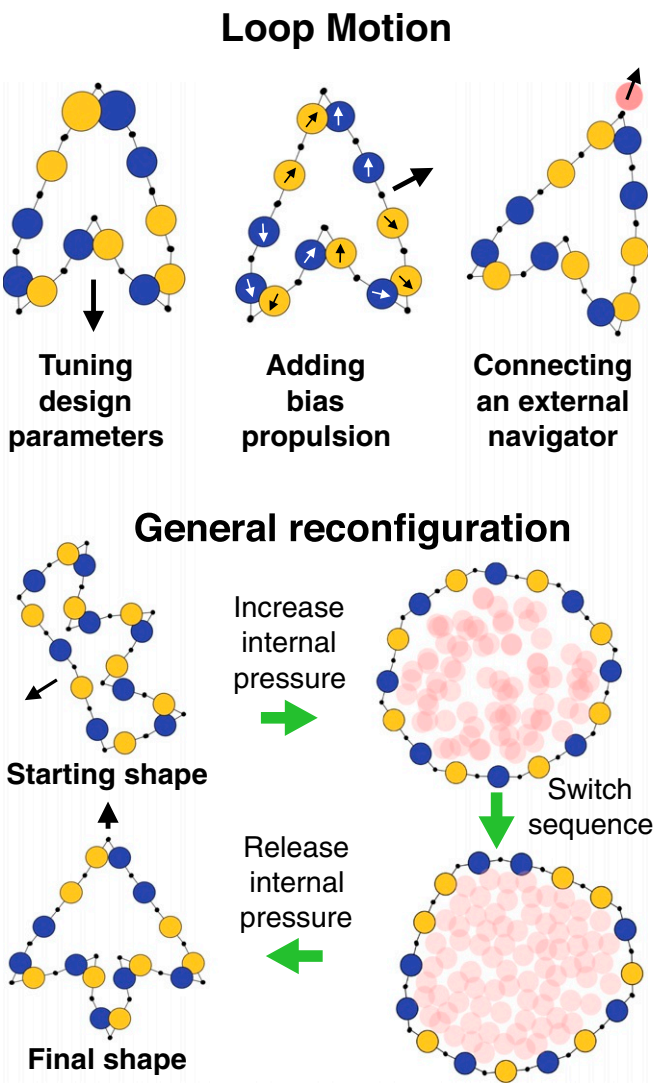

Fig. 5. Loop motion and reconfiguration. *Top* shows the simulation snapshots of examples describing three methods (*Left*, *Center*, and *Right*) for directing the motion of the folded states (Movie S7). (*Bottom*) In general reconfiguration, reconfiguration between arbitrary folded states can be accomplished by the procedure illustrated using an example (Movie S8).

Fig. 5 shows one method to achieve this general reconfiguration, through an example. Starting from an arbitrary folded shape, the internal pressure is increased to inflate the loop into the highest symmetry shape possible. Then the design parameters are switched. For the example in Fig. 5, only the sequence of motor orientations is switched. The internal pressure maintains the inflated morphology. Subsequently, the internal pressure is reduced, resulting in the new target shape. At the colloidal scale, such pressure variation can be actualized by using stimuli-responsive polymers that shrink in response to, for instance, solvent pH or salt concentration (5, 33). Alternatively, inflation of the loop may be achieved by increasing electrostatic repulsion between motors or introducing elasticity between motors.

Folding Mechanism

The three major shape features—straight segments, curved segments, and zigzags—and their arrangement in a loop to achieve a desired shape are achieved via three respective driving forces shown in Fig. 6*A*. These driving forces, in turn, are governed by the loop's design, as described below using the arrowhead example.

Straightening Force. Connected subsegments of motors acting in opposite directions stretch to form a straight geometry that is stable to mechanical perturbations. This opposing force is typically the strongest, and, therefore, folding starts by straightening of all of the segments. The size ratio of the two subsegments does not affect the straightening, although it will affect the *notching force*. The propulsion force magnitudes along a subsegment are either identical or monotonically increasing in the direction of the force. Both choices achieve straight segments within a shape, but each choice has implications for the other two folding forces. We find that a random distribution of force magnitudes over a subsegment leads to unstable folding behavior.

Curving Force. This is the net force produced along a segment when the net propulsion force of its subsegments do not cancel each other out, instead creating a curve. The degree of curvature increases with this net force (shown in *SI Appendix*, Fig. S7*A* for an example). For curved subsegments, we use linearly increasing magnitudes of the propulsion forces. Under high curvature, subsegments with identical magnitudes of propulsion forces on the motors are unstable to mechanical perturbations. In general, stabilizing higher curvatures requires higher gradients of variation in the magnitude of propulsion forces along a segment (see *SI Appendix*, Fig. S7*B* for results exploring different gradients).

Notching Force. When neighboring segments attempt to fold beyond what is permissible by steric hindrance, they bend at a corner as shown in Fig. 6*A* (third image). This bending generates a net force on the pair of corner segments, which we refer to as the notching force. In Fig. 6, we show how this driving force folds the arrowhead shape.

The loop in Fig. 6*B* is folded at $\overline{T}=0$. The figure plots torques generated at angles II, III and IV as the folding proceeds in time. Negative torque acts to reduce the angle. Folding starts by straightening the segments. Complete straightening of the segments I and II and I to IV is prevented by the larger steric hindrance between the motors at corner I. This generates a net notching force on segments I and II and I to IV, pulling them downward. This motion, in turn, reduces angles II and IV. When these angles decrease below $\pi/3$, steric hindrance prevents further folding at these angles as indicated by $\tau=0$ for $t\leq 6\ t_0$ (Fig. 6*B*). Consequently, neighboring segments bend at corners II and IV, generating net torques on segment pairs I and II and II and III, and I to IV and III to IV (see the third snapshot in Fig. 6*B*). These net torques are such that they further enforce the folding at angle III until blocked by steric hindrance for $t\leq 15\ t_0$. We measure the net torques on pairs of segments with different lengths in Fig. 6*C* by folding such pairs in simulations, connecting the ends via a harmonic bond (see *Materials and Methods*). The plot shows that such a pair always rotates from the longer to the shorter segment with a net torque proportional to their length ratio. This property explains the formation and stabilization of the arrowhead.

Although the folded state of this arrowhead is stable under stochastic (thermal) forces, it does not require the stochastic forces for folding. In Fig. 6*D*, we fold a similar loop that does not use larger motors as used above, but instead requires thermal noise. Fig. 6*D* plots torques on the shown angles of this loop similar to Fig. 6*B*. Starting from the circular configuration, all segments of this loop straighten (see first snapshot in Fig. 6*D*). No unbalanced forces are yet present in this configuration. Thermal forces cause the loop to fluctuate in configuration space around an average shape. Since the shape stiffness is at its minimum at the corners, the fluctuations are at their maximum there. The plot in Fig. 6*D* shows that angles II, III, and IV fluctuate randomly until $50\ t_0$, when the system finds the configuration containing the notching force. These torques, shown in the second snapshot in Fig. 6*D*, fold angle III inward, as indicated by negative τ_{angle} for $50\ t_0<t<100\ t_0$. Beyond $100\ t_0$, the arrowhead is stabilized, and any residual torques are due to thermal fluctuations. Thus, the role of thermal forces in this example is to explore configuration space, which is useful for folding complex shapes.

Since thermal forces control the exploration of shapes around the optimum shape in configuration space, loops at different temperatures may fold into different shapes. This behavior is shown in Fig. 6*E* (*Bottom*) for a loop with eight segments, each containing n particles. To gain insight into this behavior, we folded a pair of segments as in Fig. 6*C* and measured the net force, f_{net}, on the pair and tension, $f_{tension}$, on the bond, with length x, between end points (Fig. 6*F*). This pair corresponds to pairs of segments in Fig. 6*E* (*Bottom*). Higher temperature causes increased bending of the segments, corresponding to lower x. The two regions with $\overline{T}=0.001$ and 0.01 in Fig. 6*E* (*Bottom*) correspond to $x\gtrsim 1$ and $x<1$, respectively. Fig. 6*F* shows that $f_{tension}$ moves from positive to negative values as x moves from >1 to <1. Thus, the loop fluctuating under larger thermal forces forms pairs of segments under negative tension, whereas loops under smaller thermal forces fold differently. When $x\approx 1$, f_{net} is at its maximum. At $\overline{T}=0.001$, $x\approx 1$ for only one pair of arms, and that drives the net motion of the shape. At $\overline{T}=0.01$, every pair of arms pushes toward the center of the shape, canceling out the net motion and increasing the shape's stability. Large thermal forces result in unstable folding behavior and do not produce a unique steady-state shape (shown in Fig. 6*E*). Fig. 6*F* shows that $f_{tension}$ rapidly decreases in magnitude as n increases from 2 to 4, which corresponds to Fig. 6*E* (second column). This is because the tension on the pair at $n=4$ is not sufficient to stabilize a similar shape formed at $n=2$. Also, $f_{tension}$ saturates for $n>4$ as it does for the shape in Fig. 6*E*, corroborating the influence of the notching force on the folded state.

Quantifying Stability of the Folded State

For nonzero thermal force, different shapes exhibit different shape fluctuations in steady state. To estimate these fluctuations, we apply linear stability analysis (34) on the rotational degrees of freedom of the loop. The analytical solution $\dot{\boldsymbol{\theta}}=f(\boldsymbol{\theta})$ is approximated in the linear limit to obtain $\delta\dot{\boldsymbol{\theta}}=F\ \delta\boldsymbol{\theta}$, where vector $\boldsymbol{\theta}$ contains particle orientation and F is the Jacobian matrix calculated for the steady state (at $\overline{T}=0$) loop shape (see *Theory*). Fig. 7*A* plots the eigenvalues of F for different shapes. For

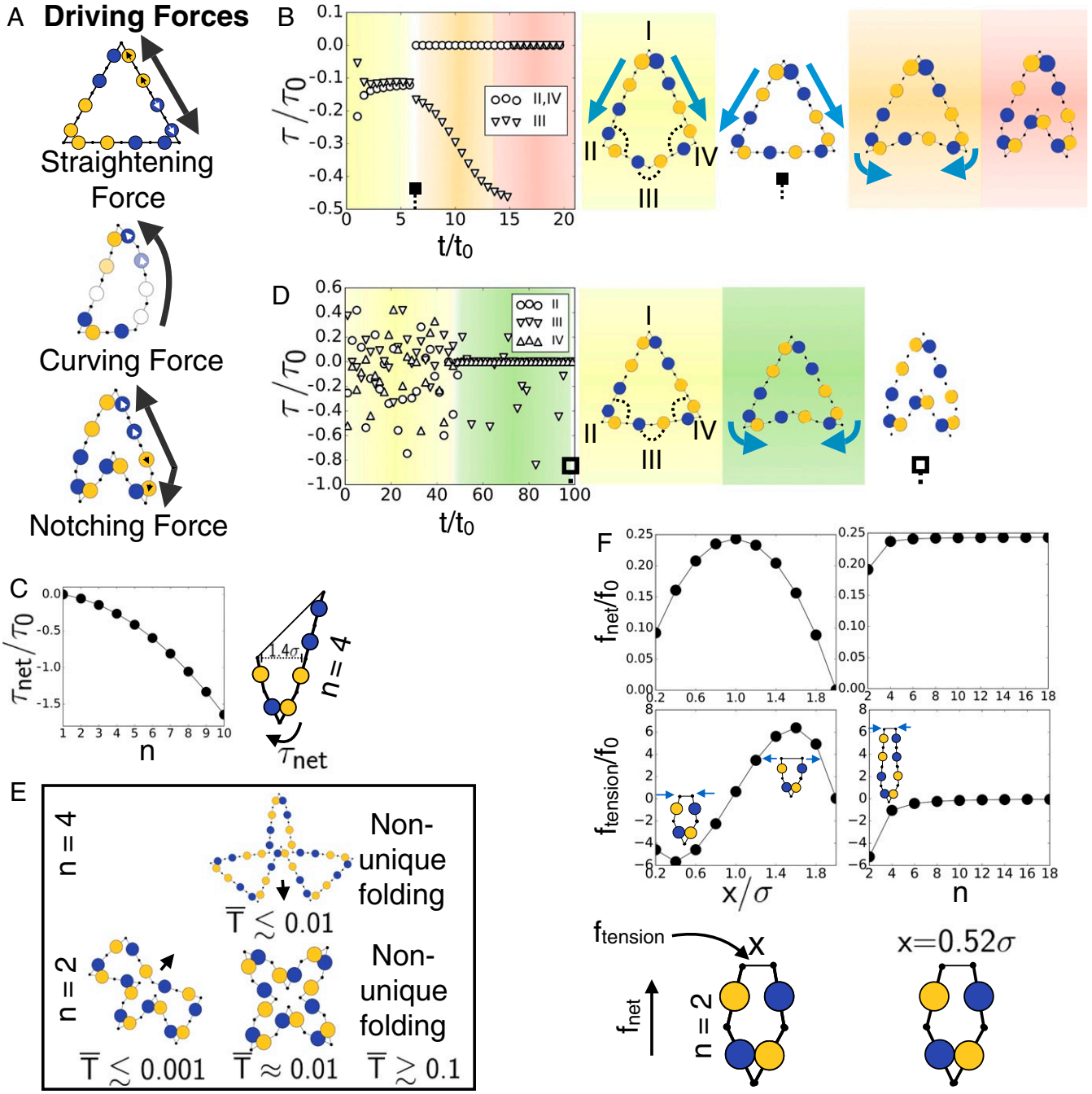

Fig. 6. Folding mechanism. (*A*) The three driving forces that drive the folding are indicated via arrows over one of the segments for each shape. (*B*) Plot of torque on the angles II, III, and IV (indicated via dotted lines) for the shown loop's simulation. The representative loop configurations at separate times are shown with their notching force (blue arrows). Negative torque decreases the angle. The shown loop is simulated at $\overline{T} = 0$ with propulsion strengths 10 f_0 for all motors. The two larger motors are of size 0.6 σ. The torque is calculated as $\gamma\ \Delta\dot{\theta}$, where $\Delta\dot{\theta}$ is the difference between rotational velocities of the two corresponding motors. Rotational velocities are calculated using the analytical solution $\dot{\theta} = f(\theta)$, where θ is obtained from the simulation. (*C*) Shown schematic is a pair of segments with ends tied by a harmonic bond of coefficient 0.01 k_0. Net torque, τ_{net} (γ_r times the net rotation measured in simulations), is plotted with respect to one of the segment sizes, n. Each simulation is initialized with straight segments at angle $\pi/3$ and folded at $\overline{T} = 0$ by tightening the harmonic bond until separated by distance 1.4σ. Motors possess unit propulsion strength. (*D*) Similar to *B*, but the loop is simulated at $\overline{T} = 0.1$ and all motors are of size $\sigma/2$. (*E*) Phase diagram of an example with respect to $\overline{T}$ and n, the number of particles in each segment. *Top* and *Bottom* rows are for $n = 4$ and $n = 2$, respectively. The propulsion strength of all motors is 4 f_0. (*F*) Shown schematic is a pair of segments with ends tied by a harmonic bond of equilibrium length x and coefficient 0.01 k_0. Tension, $f_{tension}$, on this bond and net force, f_{net}, on the pair are plotted against x (fixing $n = 2$) and n (fixing $x = 0.25\ \sigma$). Forces are measured in simulations. Motors possess unit propulsion strength.

comparison purposes, the average magnitude of the propulsion force on motors within a shape is fixed. All of the eigenvalues are nonpositive, which indicates that the folding modes are either stable or neutral. Only the first shape has a neutral/floppy mode corresponding to the eigenvalue zero. Moving left to right, the number of modes with higher eigenvalues increases, suggesting reduced stability, which is also evident by the increase in fluctuations observed in simulations and plotted in Fig. 7*B*.

Discussion

Summary. We described a design strategy to build robotic machines by using constantly propelled particles, referred to as motors. By design, these motors lack onboard computation, individual identity, and memory, hence mimicking active colloids—the intended raw material for our machines. Our strategy is to hinge these motors end-to-end in a closed loop. Hinging techniques for colloidal particles largely use polymers2007 and DNA (25–27). Communication between motors is only via steric interaction and hinge constraint, due to which the system is material and environment agnostic. The loop folds into a prescribed shape and motion as encoded via six design parameters, including the sequences of motor orientations and propulsion strengths, motor size, magnitude of the stochastic forces, loop size, and internal loop pressure. These design parameters are to be regulated via external stimuli (Fig. 1*B*) to build desired robotic machines. We investigated the design space in experiments using centimeter-scale kilobots (35) to demonstrate the simplest designs requiring the fewest robots, and in colloidal-scale Brownian dynamics simulations to validate scale invariance and explore complex loop designs. By fusing multiple loops, complex shapes such as the (letter "M") and complex dynamic behavior as demonstrated in the (gripper and pacman) loops can be achieved. We described how to reverse-engineer the loop design for a given shape and provided ways to control its motion and reconfiguration. Using simulations and analytical theory—developed using rigid body dynamics—we described the folding mechanism and quantified the stability of loop configurations.

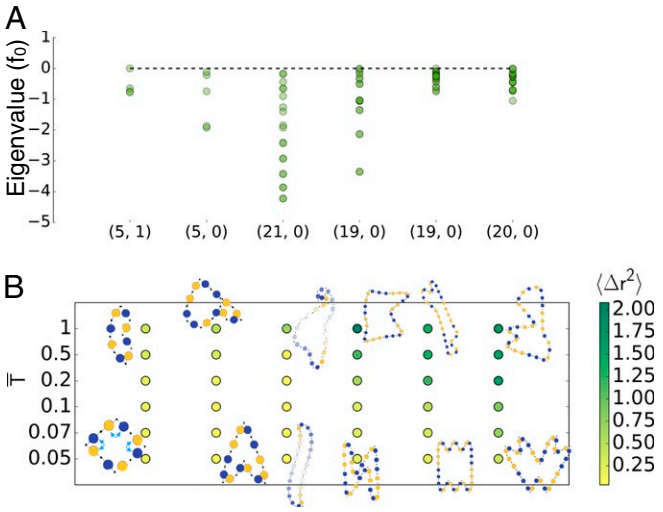

Fig. 7. Stability analysis. (*A*) Eigenvalues corresponding to the folding modes of different loop configurations are plotted. Only the first configuration—square—possesses a floppy mode. Calculated are the eigenvalues of F from the analytical solution $\delta\dot{\theta} = F\delta\theta$. The mean propulsion force of each loop is set to unity for comparison purposes. Only those eigenvalues are plotted whose eigenvectors have more than 98% projection into the kinematic space (see *Materials and Methods* for details). The values inside the brackets along the x axis are the number of folding modes and number of floppy modes. The dotted line marks the eigenvalue zero. θ corresponds to the equilibrium state. (*B*) Heatmap of average fluctuation, $\langle \Delta r^2 \rangle$, of the steady states of loops at different $\overline{T}$. $\langle \Delta r^2 \rangle$ is the difference of the distance of a motor from the shape's center-of-mass calculated between the thermal steady state and the equilibrium state, and averaged over all motors and 1,000 simulation frames. The mean propulsion of each simulated loop is set to 6 f_0. Equilibrium state is achieved by folding the shape at $\overline{T} = 0.05$ and then cooling down to $\overline{T} = 0$. Representative simulation snapshots at lower and higher $\overline{T}$ are shown. See *SI Appendix*, Fig. S8 for the complete sequence of propulsion forces.

Applications. Our loops can conceivably be refined in the future for noninvasive medical surgery where the shape of the loops can be manipulated via external fields. Since these loops are malleable, they should easily squish through delicate tissues and activate on demand using ultrasound or lasers to perform targeted diagnostics and drug delivery. Materials researchers can employ ensembles of loops to self-organize novel structures or manipulate micron-sized machine parts for bottom-up fabrication. Smart textiles can be fabricated as a metamaterial comprising a network of loop composites. *SI Appendix*, Fig. S9 illustrates several envisioned, far-future applications of our system as autonomous and user-controlled reconfigurable machines.

Future Directions. Future studies might explore numerous other variations of our design scheme. Examples include removing the constraint that all propulsion forces on robots be tangential to the loop, or tethering loops rather than having them be freely floating. The current study is limited to same-length motors. It will be interesting to vary motor lengths to tune the force coupling. Maintaining symmetry using different-length motors for the symmetrical segments of the shape will be crucial to the shape's stability. The experimental, simulation, and analytical models we provided can be easily extended for such generalized cases. Theory and simulations can find ways to improve the robustness and stability of complex loops. Breaking the planar positioning of motors is another prospect that will generate 3D loop structures. Experiments can focus on how to synthesize composites to enable complex designs and how to efficiently regulate the design space via external stimuli in order to program multiple configuration states into a single system. Another interesting anticipated experimental idea would be the synthesis of hybrid systems comprising electronics as well as nanoparticles into loops. Other interesting areas to investigate include the effects of particle–particle interactions such as attraction, repulsion, dipolar interactions, and hydrodynamics on the system.

Materials and Methods

Experiment. For experimental demonstration of our design, we use kilobots (35), bought from RoadNarrow Robotics along with a charging unit and an overhead controller. Each kilobot is 33 mm in diameter and moves using left and right motors. Each kilobot is attached at the center of a 66-mm popsicle stick. The kilobots face along the length of their popsicle sticks so that any motion of a kilobot will be always tangential to the loop at that kilobot's location. The left and right motors rotate a kilobot toward left and right, respectively, with a turn radius. This effect is exploited to propel the bots forward by alternatively actuating left and right motors (see *SI Appendix* for the microcontroller code programmed into the kilobots). The motors are manually calibrated to match the left and right rotational speeds to $\pi/5$ s^{-1}. To introduce stochasticity, the duration of the motor actuation is randomly chosen within 200 ms. Although this stochasticity is low relative to the propulsion force, it helps control the propulsion bias of the kilobots arising due to their imprecise nature. The ends of the popsicle sticks are drilled with tiny holes with cut corners (*SI Appendix*, Fig. S1). A pair of bots are connected to each other by inserting a bent pin in the corresponding holes, which allows for the folding degree of freedom. The minimum fold angle is determined by the angle of the cuts at the corners (*SI Appendix*, Fig. S1). Large variation in the propulsion force is difficult for kilobots; therefore, all motors are calibrated to exert the same force. In cases where a bot with zero propulsion is required in a loop, a popsicle stick of equal length is used in its place. Importantly, we did not use the intercommunication feature of the kilobots. Thus, the kilobots do not interact with each other other than through the mechanical forces conveyed by the popsicle sticks, and by steric constraints. All experiments were performed on a single flat surface, on which motors were calibrated and start from a circular initial configuration. Slight deviations of some shapes observed in experiments as compared to simulations are possibly due to imprecise motor calibration and approximation of the sequence.

Simulation. Each motor in a loop is modeled as a disk of diameter $\sigma/2$ with two diametrically opposite hinge ends at $\sigma/2$ distance from the

center of the disk. Volume exclusion between adjacent motors determines the minimum angle of the fold possible between them, which, in our case, is $\pi/3$. The loops are simulated in two dimensions with periodic boundary conditions using the simulation toolkit HOOMD-blue (v2.2.1) (36–40). The dynamics of motor i is simulated using the Brownian equation of motion (41).

$$\dot{\boldsymbol{r}}_i = \frac{1}{\gamma}\left(\boldsymbol{F}_i + f_i^a\,\hat{\boldsymbol{e}}_i\right) + \sqrt{2\frac{kT}{\gamma}}\,\boldsymbol{\eta}(t) \qquad [1]$$

$$\dot{\theta}_i = \tau_i/\gamma_r, \qquad [2]$$

where $\boldsymbol{r}_i$ and θ_i are the position and orientation, respectively, of motor i. $\boldsymbol{F}_i$ and τ_i are the net force and torque on i due to volume exclusion interactions and harmonic bonds. Volume exclusion is applied between disks of motors. To prevent self-intersection of a loop, volume exclusion similar to that of disks is applied between the hinges. Other than preventing the unphysical self-intersection, this force does not influence the folding dynamics. Volume exclusion interactions between centers at r distance apart are modeled via the Weeks–Chandler–Andersen potential, $U_{WCA}(r) = 4\epsilon\left[(\sigma'/r)^{12} - (\sigma'/r)^6\right] + \epsilon$, for $r < \sigma/2$, and $U_{WCA}(r) = 0$ otherwise (42), where $\sigma' = \sigma/\left(2\times 2^{1/6}\right)$ and ϵ determines the strength of the potential. We set $\epsilon = 10^{-4}k_0\,\sigma$ for our system. A hinge is modeled via harmonic bond between adjacent motors with strength k_0 and equilibrium length set to zero. The propulsion force, f_i^a, acts along $\hat{\boldsymbol{e}}_i$, which is a unit vector along the axial direction of the motor i. Hence, each f_i^a acts tangentially to the loop and will point along either the clockwise or anticlockwise direction relative to the loop. The forces and torques are nondimensionalized using $f_0 = 10^{-3}k_0\,\sigma$ and $\tau_0 = 10^{-3}k_0\,\sigma^2$, respectively. Nondimensional thermal energy $\overline{T} = kT/10^{-3}k_0\,\sigma^2$ and is set to 0.1 unless specified otherwise, and $\boldsymbol{\eta}(t)$ is unit-variance Gaussian white noise. Hinge strength is used for the nondimensionalization of forces, rather than the thermal energy, which is conventionally used for the active particle systems to quantify the propulsion sequences of the loops that fold in the nonthermal regime and compare them consistently with those that fold in the thermal regime. γ_r is the rotational drag coefficient and is set equal to the translational drag coefficient, γ. The rotational noise in a motor orientation arises from the translational diffusion of the adjacent motors bonded to it. Time is measured in units of $t_0 = \gamma/(10^{-3}k_0)$. All of the simulations are initialized from the circular configuration unless otherwise stated and equilibrated for at least 500 t_0 before measuring any quantity. Precision of folding is validated via 20 replicas each.

Theory. We use rigid body dynamics to develop the analytical solution for the loops (43). Each motor is treated as a rigid body. The joint between neighboring motors possesses rotational degree of freedom. The objective is to calculate the angular velocity vector as a function of orientation vector, $\dot{\boldsymbol{\theta}} = f(\boldsymbol{\theta})$, where $\dot{\boldsymbol{\theta}}$ and $\boldsymbol{\theta}$ contain angular velocities and orientations, respectively, of the motors in the loop. Each rigid body in two dimensions possesses two translational and one rotational degree of freedom. The force balance for the loop along each degree of freedom can be written as

$$A\boldsymbol{f}_x^J + \sum_m^M f_m^{ex}\boldsymbol{k}_x^m + \boldsymbol{f}_x^a = \Gamma\boldsymbol{v}_x \qquad [3]$$

$$A\boldsymbol{f}_y^J + \sum_m^M f_m^{ex}\boldsymbol{k}_y^m + \boldsymbol{f}_y^a = \Gamma\boldsymbol{v}_y \qquad [4]$$

$$S\left(\boldsymbol{f}_x^J + f_x^J\mathbf{1}\right) - C\left(\boldsymbol{f}_y^J + f_y^J\mathbf{1}\right) = \Gamma_r\dot{\boldsymbol{\theta}}, \qquad [5]$$

where each row corresponds to the force balance on a motor in a loop. The $\boldsymbol{f}_x^J$ and $\boldsymbol{f}_y^J$ are joint forces in x and y directions. Scalar variables f_x^J and f_y^J are added to their corresponding vectors to ensure kinematic constraints. The $\boldsymbol{v}_x$ and $\boldsymbol{v}_y$ are translational velocity vectors. The $\boldsymbol{f}_x^a$ and $\boldsymbol{f}_y^a$ are propulsion forces in x and y axes. The magnitude of volume exclusion forces between the mth pair of overlapping motors is f_m^{ex}. The $\boldsymbol{k}_x^m$ and $\boldsymbol{k}_y^m$ contain contributions per unit of f_m^{ex} in x and y directions on each motor, where this contribution is nonzero only for the motors in the mth pair and is a function of their orientations. M is the total number of overlapping pairs. The matrices A, S, C, Γ, and Γ_r are square matrices of size N, which is the number of motors in the loop.

$$A = \begin{bmatrix} 1 & -1 & 0 & \cdots & 0 & 0 \\ 0 & 1 & -1 & \cdots & 0 & 0 \\ \vdots & \vdots & \vdots & \ddots & 0 & 0 \\ 0 & 0 & 0 & \cdots & -1 & 0 \\ 0 & 0 & 0 & \cdots & 1 & -1 \\ -1 & 0 & 0 & \cdots & 0 & 1 \end{bmatrix},$$

$$S = \begin{bmatrix} \sin\theta_0 & \sin\theta_0 & 0 & \cdots & 0 & 0 \\ 0 & \sin\theta_1 & \sin\theta_1 & \cdots & 0 & 0 \\ \vdots & \vdots & \vdots & \ddots & 0 & 0 \\ 0 & 0 & 0 & \cdots & \sin\theta_{N-3} & 0 \\ 0 & 0 & 0 & \cdots & \sin\theta_{N-2} & \sin\theta_{N-2} \\ \sin\theta_{N-1} & 0 & 0 & \cdots & 0 & \sin\theta_{N-1} \end{bmatrix}.$$

C is equivalent to S but with cosine of θs. Γ is the diagonal matrix containing drag coefficients, γs, of the corresponding motors. The kinematic constraints ensuring loop connectivity during motion are given by

$$B\boldsymbol{v}_x = H_x\dot{\boldsymbol{\theta}} \qquad [6]$$

$$B\boldsymbol{v}_y = H_y\dot{\boldsymbol{\theta}}, \qquad [7]$$

where

$$B = \begin{bmatrix} 1 & 0 & 0 & \cdots & 0 & -1 \\ -1 & 1 & 0 & \cdots & 0 & 0 \\ 0 & -1 & 1 & \cdots & 0 & 0 \\ \vdots & \vdots & \vdots & \ddots & 0 & 0 \\ 0 & 0 & 0 & \cdots & 1 & 0 \\ 0 & 0 & 0 & \cdots & -1 & 1 \end{bmatrix},$$

$$H_x = -\frac{\sigma}{2}\begin{bmatrix} \sin\theta_0 & 0 & 0 & \cdots & 0 & \sin\theta_{N-1} \\ \sin\theta_0 & \sin\theta_1 & 0 & \cdots & 0 & 0 \\ 0 & \sin\theta_1 & \sin\theta_2 & \cdots & 0 & 0 \\ \vdots & \vdots & \vdots & \ddots & 0 & 0 \\ 0 & 0 & 0 & \cdots & \sin\theta_{N-2} & 0 \\ 0 & 0 & 0 & \cdots & \sin\theta_{N-2} & \sin\theta_{N-1} \end{bmatrix}.$$

H_y is equivalent to H_x but with cosines of θs and the prefactor of $+\sigma/2$. Substituting vector variables v_x and v_y from Eqs. **6** and **7** into Eqs. **3** and **4** and subsequently substituting f_x^J and f_y^J into Eq. **5** yields

$$Z\,\dot{\boldsymbol{\theta}} = \sum_m^M f_m^{ex}\boldsymbol{a}_m + f_x^J\boldsymbol{b} - f_y^J\boldsymbol{c} + \boldsymbol{d}, \qquad [8]$$

where $\boldsymbol{a}_m = CA^\dagger\boldsymbol{k}_y^m - SA^\dagger\boldsymbol{k}_x^m$, $\boldsymbol{b} = S\mathbf{1}$, $\boldsymbol{c} = C\mathbf{1}$, $\boldsymbol{d} = -SA^\dagger\boldsymbol{f}_x^a + CA^\dagger\boldsymbol{f}_y^a$, and $Z = \Gamma_r - SA^\dagger\Gamma B^\dagger H_x + CA^\dagger\Gamma B^\dagger H_y$. Superscript † represents the pseudoinverse. In the rigid body formulation, there is no explicit volume exclusion potential. Wherever a pair of motors overlap, their centers are connected by a rigid rod and the motors are assumed to be pinned to each other, and rotated with the same velocity. Generally, the placement of this rigid rod is shape-dependent. To incorporate this, we substitute $\boldsymbol{\theta} = D\boldsymbol{\theta}'$, where $\boldsymbol{\theta}'$ contains $N - M$ nonredundant orientations and D is a $N \times N_M$ matrix that duplicates the required entries of $\boldsymbol{\theta}'$. Consequently, the singular value decomposition (SVD) of ZD will have a null space of size M. Ref. 44 explains the usage of SVD for evaluating kinematic and dynamic information of a network system. Let β_ms be left-singular vectors corresponding to this null space. In order to satisfy Eq. **8**, the projection of the right-hand side on each of β_m must be zero, which gives us M additional constraints,

$$\beta_m^T\left(\sum_m^M f_m^{ex}\boldsymbol{a}_m + f_x^J\boldsymbol{b} - f_y^J\boldsymbol{c} + \boldsymbol{d}\right) = 0, \text{ where } m = 0 \text{ to } M-1. \qquad [9]$$

Similarly, to satisfy kinematic constraints (Eqs. **6** and **7**), $H_x\dot{\boldsymbol{\theta}}$ and $H_y\dot{\boldsymbol{\theta}}$ must have zero projection on the left-singular vector corresponding to the null space of B, which is $\mathbf{1}$ generating two additional constraints,

$$\mathbf{1}^T H_x\dot{\boldsymbol{\theta}} = 0 \qquad [10]$$

$$\mathbf{1}^T H_y\dot{\boldsymbol{\theta}} = 0. \qquad [11]$$

Finally, $\dot{\boldsymbol{\theta}}$ is calculated using Eqs. **8**–**11**.

To measure stability of a loop shape around its steady-state value, we use linear stability analysis (34), where Eqs. **3**–**7** are approximated in the linear limit. Overlapping particles are assumed to fluctuate together in the linear limit. By applying similar derivation as above, $\delta\dot{\theta'} = F\delta\theta'$ is evaluated, where F is the Jacobian matrix and $\delta\theta'$ contains $N-M$ nonredundant entries. To remove any global rotation, we fix the first motor to be stationary by substituting $\theta' = \begin{bmatrix} \mathbf{0_{N-1}}^T \\ I_{N-1} \end{bmatrix} \theta''$, where θ'' contains orientations 1 to $N-M-1$, resulting in $\delta\dot{\theta''} = F'\delta\theta''$. The eigenvalue decomposition of F' yields stable, unstable, and neutral (floppy) folding modes corresponding to negative, positive, and zero eigenvalues. However, the motion defined by an eigenvector of F' may be geometrically forbidden. Therefore, to identify feasible eigenvectors, we calculate the kinematic space of a loop, which is of rank $N-M-2$ (which includes the global rotation mode). The kinematic matrix is given by $V_{kinematic} = V\mathcal{N}$, where column vectors are the basis vectors. V contains the right-singular vectors of $\begin{bmatrix} B & 0_N \\ 0_N & B \end{bmatrix} \begin{bmatrix} H_x D \\ H_y D \end{bmatrix}$ excluding its null space, and $\mathcal{N}$ is the null space of SVD of $\begin{bmatrix} \mathbf{1_N}^T & \mathbf{0_N}^T \\ \mathbf{0_N}^T & \mathbf{1_N}^T \end{bmatrix} \begin{bmatrix} H_x D \\ H_y D \end{bmatrix} V$.

All data as well as simulation, analysis, and visualization scripts are publicly available at https://doi.org/10.7302/czgw-2x26. The software used to perform the simulations is publicly available at https://github.com/glotzerlab/hoomd-blue.

ACKNOWLEDGMENTS. This work was supported as part of the Center for Bio-Inspired Energy Science, an Energy Frontier Research Center funded by the US Department of Energy, Office of Science, Basic Energy Sciences under Award DE-SC0000989. Our computational resources are supported by Advanced Research Computing at the University of Michigan, Ann Arbor.

1. B. J. Nelson, I. K. Kaliakatsos, J. J. Abbott, Microrobots for minimally invasive medicine. *Annu. Rev. Biomed. Eng.* **12**, 55–85 (2010).
2. E. Şahin, *Swarm Robotics: From Sources of Inspiration to Domains of Application in Swarm Robotics* (Springer, Berlin, Germany, 2005), pp. 10–20.
3. E. Diller, M. Sitti, Micro-scale mobile robotics. *Found. Trends Rob.* **2**, 143–259 (2011).
4. S. Goldstein, J. Campbell, T. Mowry, Programmable matter. *Computer* **38**, 99–101 (2005).
5. S. Palagi, P. Fischer, Bioinspired microrobots. *Nat. Rev. Mater.* **3**, 113–124 (2018).
6. G. Z. Yang *et al.*, The grand challenges of science robotics. *Sci. Robo.* **3**, eaar7650 (2018).
7. M. Guix, C. C. Mayorga-Martinez, A. Merkoçi, Nano/micromotors in (Bio)chemical science applications. *Chem. Rev.* **114**, 6285–6322 (2014).
8. C. Bechinger *et al.*, Active particles in complex and crowded environments. *Rev. Mod. Phys.* **88**, 045006 (2016).
9. M. C. Marchetti *et al.*, Hydrodynamics of soft active matter. *Rev. Mod. Phys.* **85**, 1143–1189 (2013).
10. S. Sabrina *et al.*, Shape-directed microspinners powered by ultrasound. *ACS Nano* **12**, 2939–2947 (2018).
11. A. M. Maier *et al.*, Magnetic propulsion of microswimmers with DNA-based flagellar bundles. *Nano Lett.* **16**, 906–910 (2016).
12. D. Walker, B. T. Käsdorf, H. H. Jeong, O. Lieleg, P. Fischer, Enzymatically active biomimetic micropropellers for the penetration of mucin gels. *Sci. Adv.* **1**, e1500501 (2015).
13. J. Palacci, S. Sacanna, A. P. Steinberg, D. J. Pine, P. M. Chaikin, Living crystals of light-activated colloidal surfers. *Science (New York, N.Y.)* **339**, 936–940 (2013).
14. B. L. Feringa, The art of building small: From molecular switches to motors (Nobel Lecture). *Angew. Chem. Int. Ed.* **56**, 11060–11078 (2017).
15. B. Yurke, A. J. Turberfield, A. P. Mills, F. C. Simmel, J. L. Neumann, A DNA-fuelled molecular machine made of DNA. *Nature* **406**, 605–608 (2000).
16. T. Yu et al., Chemical micromotors self-assemble and self-propel by spontaneous symmetry breaking. *Chem. Commun.* **54**, 11933–11936 (2018).
17. M. Agrawal, I. R. Bruss, S. C. Glotzer, Tunable emergent structures and traveling waves in mixtures of passive and contact-triggered-active particles. *Soft Matter* **13**, 6332–6339 (2017).
18. M. Rubenstein, A. Cornejo, R. Nagpal, Robotics. Programmable self-assembly in a thousand-robot swarm. *Science (New York, N.Y.)* **345**, 795–799 (2014).
19. M. F. Hagan, A. Baskaran, (2016) Emergent self-organization in active materials.arXiv:1602.0388 (10 February 2016).
20. J. W. Boley *et al.*, Shape-shifting structured lattices via multimaterial 4D printing. *Proc. Natl. Acad. Sci. U.S.A.* **116**, 20856–20862 (2019).
21. S. Li *et al.*, Particle robotics based on statistical mechanics of loosely coupled components. *Nature* **567**, 361–365 (2019).
22. I. Slavkov *et al.*, Morphogenesis in robot swarms. *Sci. Robo.* **3**, eaau9178 (2018).
23. L. Giomi, N. Hawley-Weld, L. Mahadevan, Swarming, swirling and stasis in sequestered bristle-bots. *Proc. Math. Phys. Eng. Sci.* **469**, 20120637 (2013).
24. G. A. Devries *et al.*, Divalent metal nanoparticles. *Science (New York, N.Y.)* **315**, 358–361 (2007).
25. D. Nykypanchuk, M. M. Maye, D. van der Lelie, O. Gang, DNA-guided crystallization of colloidal nanoparticles. *Nature* **451**, 549–552 (2008).
26. C. Zhang et al., A general approach to DNA-programmable atom equivalents. *Nat. Mater.* **12**, 741–746 (2013).
27. W. B. Rogers, W. M. Shih, V. N. Manoharan, Using DNA to program the self-assembly of colloidal nanoparticles and microparticles. *Nat. Rev. Mat.* **1**, 16008 (2016).
28. A. Kaiser, S. Babel, B. Ten Hagen, C. Von Ferber, H. Löwen, How does a flexible chain of active particles swell?. *J. Chem. Phys.* **142**, 124905 (2015).
29. A. Laskar, R. Adhikari, Brownian microhydrodynamics of active filaments. *Soft Matter* **11**, 9073–9085 (2015).
30. D. Nishiguchi, J. Iwasawa, H. R. Jiang, M. Sano, Flagellar dynamics of chains of active Janus particles fueled by an AC electric field. *New J. Phys.* **20**, 015002 (2018).
31. M. Spellings *et al.*, Shape control and compartmentalization in active colloidal cells. *Proc. Nat. Acad. Sci. U.S.A.* **112**, E4642–E4650 (2015).
32. L. Hu, Q. Zhang, X. Li, M. J. Serpe, Stimuli-responsive polymers for sensing and actuation. *Mater. Horiz.* **6**, 1774–1793 (2019).
33. A. Ghosh *et al.*, Stimuli-responsive soft untethered grippers for drug delivery and robotic surgery. *Front. Mech. Eng.* **3**, 7 (2017).
34. R. Morgan, Linearization and stability analysis of nonlinear problems. *Rose-Hulman Undergrad. Math. J.* **16**, 5 (2017).
35. M. Rubenstein, C. Ahler, R. Nagpal, "Kilobot: A low cost scalable robot system for collective behaviors" in *2012 IEEE International Conference on Robotics and Automation* (Institute of Electrical and Electronics Engineers, 2012), pp. 3293–3298.
36. HOOMD-blue, Version 2.6.0. https://github.com/glotzerlab/hoomd-blue. Accessed 22 September 2019.
37. J. A. Anderson, C. D. Lorenz, A. Travesset, General purpose molecular dynamics simulations fully implemented on graphics processing units. *J. Comput. Phys.* **227**, 5342–5359 (2008).
38. J. Glaser *et al.*, Strong scaling of general-purpose molecular dynamics simulations on GPUs. *Comput. Phys. Commun.* **192**, 97–107 (2015).
39. T. D. Nguyen, C. L. Phillips, J. A. Anderson, SC. Glotzer, Rigid body constraints realized in massively-parallel molecular dynamics on graphics processing units. *Comput. Phys. Commun.* **182**, 2307–2313 (2011).
40. C. L. Phillips, J. A. Anderson, S. C. Glotzer, Pseudo-random number generation for Brownian dynamics and dissipative particle dynamics simulations on GPU devices. *J. Comput. Phys.* **230**, 7191–7201 (2011).
41. M. P. Allen, D. J. Tildesley, *Computer Simulation of Liquids* (Oxford University Press, 1989).
42. D. Chandler, J. D. Weeks, H. C. Andersen, Van der Waals picture of liquids, solids, and phase transformations. *Science (New York, N.Y.)* **220**, 787–94 (1983).
43. R. Featherstone, D. Orin, Robot dynamics: Equations and algorithms" in *Proceedings 2000 ICRA. Millennium Conference. IEEE International Conference on Robotics and Automation. Symposia Proceedings* (Institute of Electrical and Electronics Engineers), vol. 1, pp. 826–834.
44. S. Pellegrino, Structural computations with the singular value decomposition of the equilibrium matrix. *Int. J. Solid Struct.* **30**, 3025–3035 (1993).